

Ultrahigh fuel utilization in polymer electrolyte fuel cells – Part II: A modeling study

Yun Wang, Xiaoguang Yang & Chao-Yang Wang

To cite this article: Yun Wang, Xiaoguang Yang & Chao-Yang Wang (2021): Ultrahigh fuel utilization in polymer electrolyte fuel cells – Part II: A modeling study, International Journal of Green Energy, DOI: [10.1080/15435075.2021.1941042](https://doi.org/10.1080/15435075.2021.1941042)

To link to this article: <https://doi.org/10.1080/15435075.2021.1941042>



Published online: 29 Jun 2021.



Submit your article to this journal [↗](#)



View related articles [↗](#)



View Crossmark data [↗](#)



Ultrahigh fuel utilization in polymer electrolyte fuel cells – Part II: A modeling study

Yun Wang, Xiaoguang Yang, and Chao-Yang Wang 

Electrochemical Engine Center (ECEC), and Department of Mechanical and Nuclear Engineering, The Pennsylvania State University, University Park, PA USA

ABSTRACT

In this paper, ultrahigh fuel utilization (>98%) in polymer electrolyte fuel cells (PEFCs) is numerically studied to investigate three aspects for this operation strategy: its effect on fuel cell performance, occurrence of fuel starvation, and altered water management. Simulation results reveal that the anode flow, when using pure hydrogen fuel, decelerates to nearly zero under the high fuel utilization. The anode gas flow remains high in the hydrogen concentration throughout the gas flow channel, eliminating concerns of fuel starvation and increased anode overpotential. The numerical study confirms the experimental observation that the high-fuel-utilization strategy has very little impact on cell power output in the stable operating regime. It is shown that fuel cell's water removal almost totally relies on the cathode channel flow under ultrahigh fuel utilization, which may be one cause for experimentally observed instability in fuel cell operation under low current density.

ARTICLE HISTORY

Received 3 February 2021
Accepted 24 May 2021

KEYWORDS

Fuel cells; fuel utilization; hydrogen; low stoichiometry; modeling; water management

1. Introduction

The advantage of ultrahigh fuel utilization (>98%) in PEFCs is apparent in practice: it eliminates the recirculation system, meanwhile maintains the efficiency of fuel usage, thereby reducing parasitic power and increasing reliability. This strategy is especially attractive in the transportation application. However, it may have a few concerns: the first is the adverse effect of ultrahigh fuel utilization on the cell performance. Since all the hydrogen are nearly consumed, local hydrogen shortage may occur and increase the overpotential, thereby decreasing cell performance (Larminie, Dicks, and McDonald 2003). Another concern is occurrence of fuel starvation due to high fuel utilization. One consequence of fuel starvation is the water electrolysis in the anode (>1.23 V) when hydrogen gas becomes unavailable. It may cause the oxidation of the support carbon in the electrode, thereby permanently damaging the catalyst layer (>1.4 V) (Knight et al. 2004; Wilkison and St-Pierre 2003). In addition, water management in fuel cell can be a concern because water removal may totally rely on the cathode channel flow.

Another concept that has been proposed to eliminate the hydrogen fuel recirculation is the dead-ended anode design for PEFCs, in which there are no anode outlets so that all the hydrogen are consumed by the fuel cell reactions (Jang et al. 2015; Kurnia, Sasmito, and Shamim 2019; Wang 2004). However, chemical degradations including carbon corrosion in the catalyst layer and membrane decomposition were reported for the dead-ended anode design (McKahn 2015). It was observed that nitrogen and water may accumulate in fuel cells, causing severe cell performance decline and fluctuations (Matsuura et al. 2011). Different with the dead-ended design, which has 100% fuel utilization, the proposed ultrahigh fuel

utilization has an open anode outlet, permitting the very small amount of unused hydrogen and other species from crossover to be removed out of the anode channel. This strategy mitigates the nitrogen and water accumulation in the anode.

To numerically study ultrahigh fuel utilization, the PEFC model needs to account for a few fundamental mechanisms that describe fuel cell operation, anode hydrogen flow physics, and water transport phenomena. First, due to the significant variation in the anode flow, the model must accurately describe the gas flow field, such as large changes in the gas flow density and velocity. Second, since the anode overpotential may considerably affect cell performance, the electrochemical kinetics in the anode catalyst layer needs to be precisely incorporated. Third, the unique water management demands a precise description of water transport in the electrolyte membrane, such as the electro-osmotic drag and back-diffusion of water.

PEFC models have been developed through decades and have been a rapidly growing field of research in the study of the area (Demuren and Edwards 2020; Wang et al. 2011; Yang et al. 2017). Obviously, one-dimensional models, which mostly targeted at the out-of-plane dimension, are unsuitable to the detailed study on ultrahigh fuel utilization. Two-dimensional models may be applicable if the along-channel gas flows are incorporated to the models. However, due to lack of the third physical dimension, it is difficult to compare and validate with experimental data. Three-dimensional (3D) models were proposed by many early studies (Song and Meng 2013; Sun et al. 2012; Wang and Wang 2006a, 2005a) (to list just a few). Some of them neglected a detailed water transport model in the electrolyte membrane by assuming the membrane as an interface. Büchi and Scherer (Büchi and Scherer 2001) experimentally showed a strongly non-linear water content profile prevailing in the Nafion® membrane, and Kulikovskiy (2003) and Wang and

Wang (2006b) numerically demonstrated the paramount importance of accounting for non-linear water transport through the membrane. In addition, some 3D models (Wang and Wang 2006a, 2005a) assume a constant flow condition in the gas flow channels, which make it difficult to predict ultrahigh fuel utilization. Several studies (Springer et al. 2001; Wang and Wang 2006b; Yang et al. 2017) incorporated a detailed description of transport mechanisms in the MEA, such as the electrolyte potential behavior and non-linear water transport through the membrane. Wang and Wang (2005b) took into account a rigorous description of the reactive gas flow features in their model to capture the large gas density and velocity variations arising from the electrochemical reactions. These features are essential to the study of this extreme condition, i.e. ultrahigh fuel utilization, in which the anode hydrogen gas flow is anticipated to be decelerated to around 0 at the outlet. Additionally, the model contains detailed 3D submodels of water transport in the membrane and electrochemical behaviors in the catalyst layers. These model features are essential to studying the targeted concerns associated with this strategy, i.e. occurrence of local hydrogen starvation, reduced fuel cell performance, and altered water management. For modeling effort in nonisothermal or two-phase flow approaches, readers are referred to Goshtasbi, Pence, and Ersal (2016), Kone et al. (2017), Yang et al. (2017), and Zhou et al. (2017).

The objective of this work is to employ the 3D fuel cell model (Wang and Wang 2005b) to investigate the ultrahigh fuel utilization strategy under dry operation using the anode stoichiometry = 1.01 for a case study. The numerical study revealed the detailed distributions of the gas flow, hydrogen and water vapor in fuel cells, predicted/validated the fuel cell performance, and

explained the experimental observation for the ultrahigh fuel utilization strategy. Future work will incorporate the two-phase flow submodel to study operation instability.

2. Physical and numerical model

In the numerical study, we consider steady state operation. A few assumptions are made in the PEFC model: (1) ideal gas mixtures; (2) isotropic and homogeneous membrane, catalyst layers, and gas diffusion media; (3) laminar flow due to small pressure gradients and flow velocity; (4) equilibrium between ionomer and surrounding fluid in the catalyst layers; (5) isothermal condition; and (6) water exists in vapor phase or very small droplets mixed with gas flows. The model consists of four principles of conservation: mass, momentum, species and charge (Wang and Wang 2005b):

$$[\text{Continuity : } \nabla \cdot \rho \vec{u} = S_m] \quad (1)$$

$$[\text{Momentum : } \frac{1}{\varepsilon^2} \nabla \cdot (\rho \vec{u} \vec{u}) = - \nabla p + \nabla \cdot \tau + S_u] \quad (2)$$

$$\text{Species : } \varepsilon \frac{\partial \rho m_k}{\partial t} + \nabla \cdot (\rho \vec{u} m_k) = \nabla \cdot (\rho D_k^{eff} \nabla m_k) + S_k \quad (3)$$

$$\text{Charge : } 0 = \nabla \cdot (\kappa^{eff} \nabla \Phi_e) + S_\phi \quad (4)$$

where \vec{u} is the superficial velocity in the porous media and the variable mixture density can be expressed as the function of molar concentrations of the components:

Table 1. Physical and transport properties (Wang et al. 2011; Wu 2016; Yang et al. 2017).

Quantity	Value
Water saturation pressure, p^{sat} (Pa)	$\log_{10} p^{sat} = -2.1794 + 0.02953 (T-273.15) - 9.1837 \times 10^{-5} (T-273.15)^2 + 1.4454 \times 10^{-7} (T-273.15)^3$
Water activity, a	$a = \frac{c_w RT}{p^{sat}}$
Membrane water content, λ (H ₂ O/S O ₃ ⁻)	$(0.005139\lambda - 0.00326) \exp[1268(\frac{1}{303} - \frac{1}{T})]$
Ionic conductivity of membrane, κ (S/cm)	
H ₂ O diffusivity in membrane, D_w^m (cm ² /s)	$D_w^m = \begin{cases} 3.1 \times 10^{-3} \lambda (e^{0.28\lambda} - 1) \cdot e^{-2346/T} & \text{for } \lambda \leq 3 \\ 4.17 \times 10^{-4} \lambda (1 + 161e^{-\lambda}) \cdot e^{-2346/T} & \text{otherwise} \end{cases}$
Electroosmosis coefficient, n_d (H ₂ O/H ⁺)	$n_d = \begin{cases} 1.0 & \text{for } \lambda \leq 14 \\ \frac{1.5}{8} (\lambda - 14) + 1.0 & \text{otherwise} \end{cases}$
Membrane density, ρ (kg/m ³)	
O ₂ diffusivity in membrane (cm ² /s)	1.22×10^{-6}
Gas diffusion coefficient in porous media, D^{eff} (cm ² /s)	$D^{eff} = \varepsilon^{1.5} D$
Diffusivity in the gas channels, D (cm ² /s) (2006)	$D_o (\frac{T}{353})^{3/2} (\frac{1}{p})$
H ₂ /H ₂ O diffusivity in anode gas at standard condition, $D_{o,H_2,a}/D_{o,w,a}$ (m ² /s)	$1.1028 \times 10^{-4} / 1.1028 \times 10^{-4} \text{ m}^2/\text{s}$
O ₂ /H ₂ O diffusivity in cathode gas at standard condition, $D_{o,O_2,c}/D_{o,w,c}$ (m ² /s)	$3.2348 \times 10^{-5} / 7.35 \times 10^{-5} \text{ m}^2/\text{s}$
Viscosity of anode/cathode gas, μ (kg/m s) (Bergman et al. 2011)	$\mu = 9.88 \times 10^{-6} X_{H_2} + 1.12 \times 10^{-5} X_{H_2O} + 2.01 \times 10^{-5} X_{N_2} + 2.3 \times 10^{-5} X_{O_2}$

Table 2. Source terms for the conservation equations in each region (Wang and Wang 2005b).

	S_u	S_k	S_φ	S_m
Gas channels	0	0	-	0
Diffusion layers	$-\frac{\mu}{K_{DL}} \vec{u}$	0	0	0
Catalyst layer	$-\frac{\mu}{K_{CL}} \vec{u}$	$-\left(\frac{n_d}{F} i_e\right) - \frac{s_{kj}}{n_k F}$	j	$-\sum_k \left(M_k \frac{s_{kj}}{n_k F}\right) - M_w \cdot \left(\frac{n_d}{F} i_e\right) + M_w (D_{w,m} C_w)$
Membrane	$-\frac{\mu}{K_m} \vec{u}$	0	0	-

Note: n_d is the electroosmotic drag coefficient for water. For H_2 and O_2 , $n_d = 0$.

Table 3. Electrochemical properties.

Description	Anode	Cathode
Transfer current density, j (A/m ²)	$a_{i_{0,a}} \left(\frac{C_{H_2}}{C_{H_2,ref}}\right)^{1/2} \left(\frac{a_a + a_c}{RT} \cdot F \cdot \eta\right)$	$-a_{i_{0,c}} \left(\frac{C_{O_2}}{C_{O_2,ref}}\right) \exp\left(-\frac{a_c F}{RT} \cdot \eta\right)$
Surface overpotential, η (V)	$\Phi_s - \Phi_e - U_o$ (with $\Phi_s = 0$)	$\Phi_s - \Phi_e - U_o$ (with $\Phi_s = V_{cell}$)
Equilibrium potential, U_o (V)	0	$1.23 - 0.9 \times 10^{-3} (T - 298)$
Exchange current density \times reaction surface area, a_{i_0} (A/m ²)	1.0×10^9	9000
Transfer coefficient, α	$\alpha_a + \alpha_c = 2$	$\alpha_c = 1$

$$\rho = \frac{P}{RT \sum (m_k/M_k)} \quad (5)$$

We choose Eq. (3) to solve for water and oxygen molar concentrations, and then calculate the concentrations of hydrogen and nitrogen by the ideal gas law:

$$m_{H_2/N_2} = 1 - \sum_{k=others} m_k \quad (6)$$

The model equations and their physical, transport, and electrochemical properties are summarized in Table 1-3 in detail, where the molar concentration, C_k , of species is determined by

$$C_k = \frac{\rho m_k}{M_k} \quad (7)$$

Boundary conditions- Seven unknowns, including \vec{u}, P, m_{O_2}, m_w and φ_e , are involved in the coupled differential equations, Eqs. (1) through (4), that require boundary conditions.

2.1. Flow Inlets

The inlet velocity \vec{u}_{in} in a gas channel is expressed by the respective

stoichiometric flow ratio, i.e., ξ_a or ξ_c defined at the reference current density, I_{ref} , as

$$\xi_a = \frac{C_{H_2}^a u_{in,a} A_a}{I_{ref} A} \quad \text{and} \quad \xi_c = \frac{C_{O_2}^c u_{in,c} A_c}{I_{ref} A} \quad (8)$$

where A_a and A_c are the flow cross-sectional areas of the anode and cathode gas channels, respectively, and $u_{in,a}$ and $u_{in,c}$ the inlet velocities of the gas flow channels. The inlet molar concentrations, C_k^a and C_k^c , are determined by the inlet pressure and humidity according to the ideal gas law.

2.2. Outlets

Fully developed or no-flux conditions are applied:

$$\frac{\partial \vec{u}}{\partial n} = 0, \quad \frac{\partial m_k}{\partial n} = 0, \quad \frac{\partial \varphi_e}{\partial n} = 0 \quad (9)$$

2.3. Walls

No-slip and impermeable velocity condition and no-flux conditions are applied:

$$\vec{u} = 0, \quad \frac{\partial m_k}{\partial n} = 0, \quad \frac{\partial P}{\partial n} = 0, \quad \frac{\partial \varphi_e}{\partial n} = 0 \quad (10)$$

Numerical procedures: The governing equations are solved by the commercial CFD (computational fluid dynamics) software packages, Star-CD[®], with SIMPLE (semi-implicit pressure linked equation) algorithm (Patankar 1980). The source terms and physical properties are incorporated into the user-defined subroutine, based on the software's user-coding capability. The computational domain of the single-channel PEFC is shown in Figure 1. The geometrical and operational parameters are listed in Table 4. About 100,000 ($51 \times 100 \times 20$) computational cells are used to capture the complex electrochemical and physical processes occurring in PEFCs during operation. In addition, overall species balance is checked besides the equation residuals as an important convergence criterion. These species balance checks ensure physically meaningful results to be obtained. In all the simulations to be presented in the next section, values of species mass imbalance (i.e. O_2 and H_2O) are less than 0.1%.

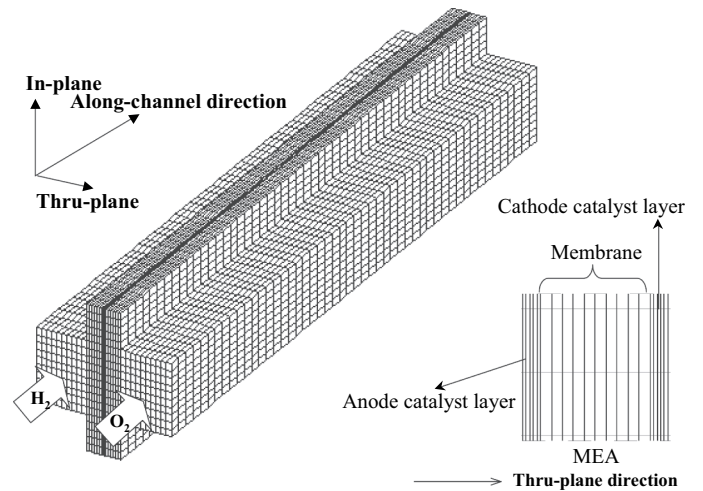
**Figure 1.** Computational domain and mesh of the single-channel PEFC.

Table 4. Geometrical and operating parameters.

Quantity	Value
Gas channel depth/ width	1.0/1.0 mm
Shoulder width	1.0 mm
GDL thickness, δ_{GDL}	0.3 mm
Catalyst layer thickness, δ_{CL}	0.01 mm
Membrane (N112) thickness, δ_m	0.03 mm
Fuel cell height/length	2.0/100.0 mm
Anode/cathode inlet pressures, P	2.0/2.0 atm
Cathode stoichiometry (stoich _c), ξ_c	2.0
Cell voltage, V_{cell}	0.7 V
Temperature of fuel cell, T	353 K
Relative humidification of anode/cathode injection	50/0%
Porosity of diffusion layers, ϵ	0.6
Porosity of catalyst layers, ϵ_g	0.4
Volume fraction of ionomer in catalyst layers, ϵ_m	0.2
Permeability of diffusion layers, K_{GDL}	10^{-12} m^2
Permeability of catalyst layers, K_{CL}	10^{-15} m^2

3. Results and Discussion

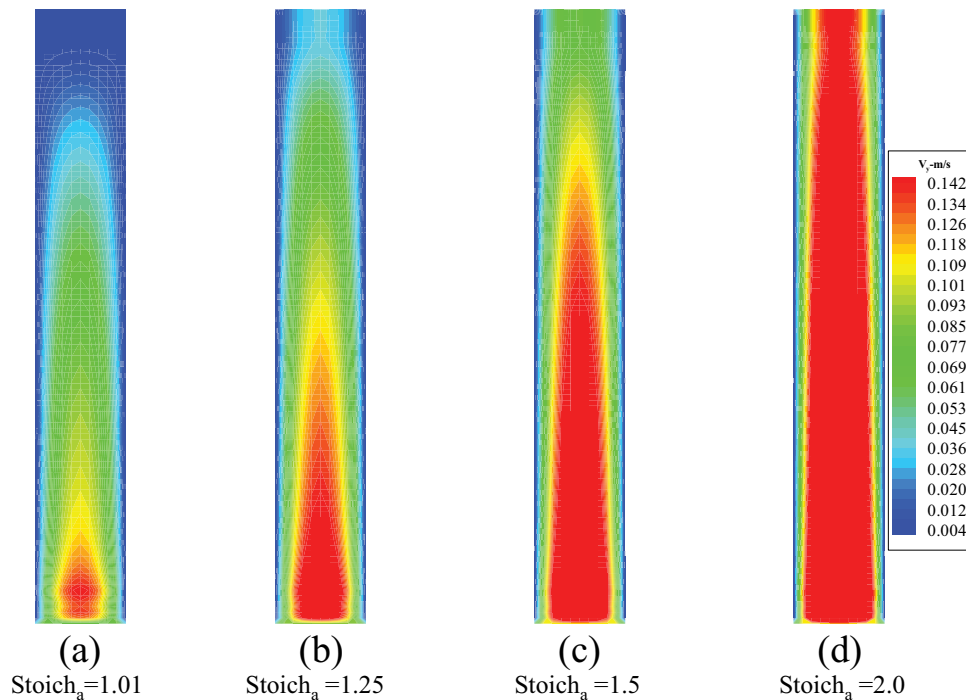
To clearly illustrate the water transport in fuel cell, a dry case, i.e. $RH_{a/c} = 50/0\%$, was chosen to investigate ultrahigh fuel utilization where the anode flow encounters large variations in both flow rate and gas density. Other anode stoichiometries were simulated as well for comparison and exploring the unique features of ultrahigh fuel utilization. Figures 2–8 present the simulation results for stoich_a = 1.01, 1.25, 1.5, and 2.0 under 0.7 V. The predicted current densities are listed in Table 5, which shows that the current density declines slightly when decreasing the stoich_a, specifically the current output is reduced by 10% when the stoich_a decreases from 2.0 to 1.01.

Figure 2 presents the gas axial velocity at the mid-depth of the anode channel and shows that all the hydrogen gas velocities decrease down the channel. The decelerated mass flow is caused by the hydrogen consumption in the anode catalyst layer. Near the outlet, the anode flow decelerates to a level of

0.001 m/s for stoich_a = 1.01, indicating that almost all hydrogen is consumed under the ultrahigh fuel utilization. As to stoich_a = 2.0 (i.e. only 50% of hydrogen gas was consumed by the fuel cell), there exists a strong anode outflow at the outlet; thus, the unused hydrogen gas needs to be collected and sent back to the anode inlet via a recycling unit. For the other two cases, a certain amount of hydrogen fuel was flowed out of the outlet; thus, a recycling unit is in need for the unused hydrogen.

Figure 3 presents the water vapor concentration at the mid-depth of the anode channel, showing that the water contours are similar to each other despite the difference in the anode stoichiometry. This is due to the fact that the water profile in a fuel cell is primarily determined by the cathode air stream that is capable of holding several times more water vapor than the anode stream. Minor distinction is presented for the low-water-content (or the blue) region: the low-value (or the blue) region expands as the stoich_a decreases. This can be explained by the fact that the lower-stoich_a anode flow contains less amount of water ($RH = 50\%$ in the anode) to compensate the water loss to the cathode due to the electroosmotic drag.

The effect of the decelerated anode stream on the hydrogen content is presented by Figure 4, which shows the hydrogen distribution at the mid-depth of the anode channel. From Table 5, the difference among the output current densities is within 10%; thus, the hydrogen fuel consumption rates are similar within 10% in difference. Figure 4 shows that the hydrogen concentrations are similar and maintain high, even for the ultrahigh fuel utilization condition. The primary reason is that pure hydrogen gas is used. In other words, though about 99% fuel is consumed under the ultrahigh fuel utilization case, the anode flow deceleration leads to the species accumulation by convection. The presence of the high hydrogen concentration in the entire anode gas flow channel waves the concerns of potential fuel starvation and the increased anode overpotential.

**Figure 2.** Axial velocity distribution at the mid-depth of the anode channel for stoich_a = 1.01, 1.25, 1.5, and 2.0 at 0.7 V and $RH_{a/c} = 50\%/0\%$.

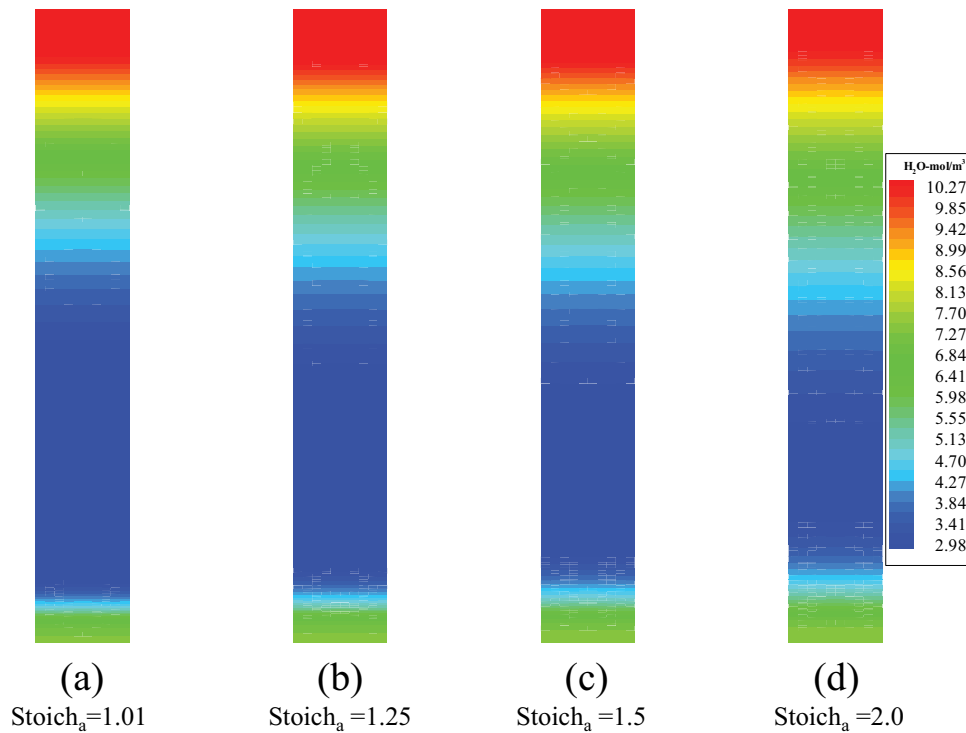


Figure 3. Water vapor distribution at the mid-depth of the anode channel for $\text{stoich}_a = 1.01, 1.25, 1.5,$ and 2.0 at 0.7 V and $\text{RHa}/c = 50\%/0\%$.

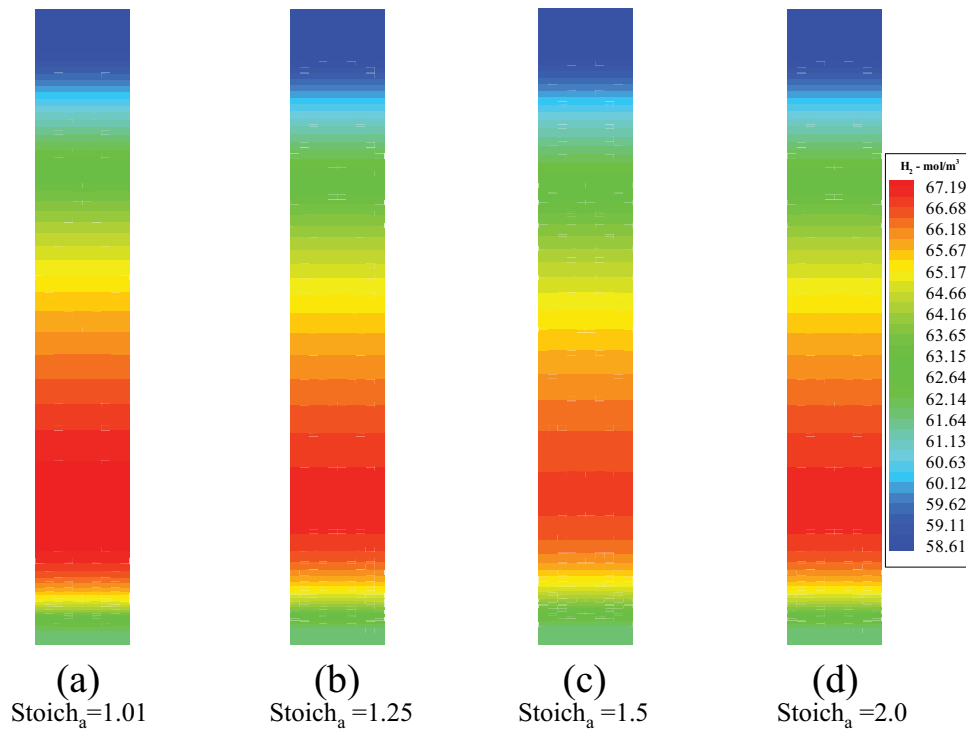


Figure 4. Hydrogen distribution at the mid-depth of the anode channel for $\text{stoich}_a = 1.01, 1.25, 1.5,$ and 2.0 at 0.7 V and $\text{RHa}/c = 50\%/0\%$.

The fuel cell's local performance is shown in Figure 5, which presents the current density contours in the MEA. First, it shows that the current density distributions are similar among the four cases, indicative of no significant adverse effect on cell performance for the ultrahigh fuel utilization. Second, minor distinctions appear in the low-current-density (or blue) regions: the low-value (or blue)

band expands as the stoich_a decreases. This can be easily explained by Figure 3, which shows a similar trend of water distribution. Note that Figure 4 indicates a high hydrogen concentration and hence a similar anode overpotential for all the four cases. In addition, the high-current-density region near the outlet is smaller under the ultrahigh fuel utilization case than the others.

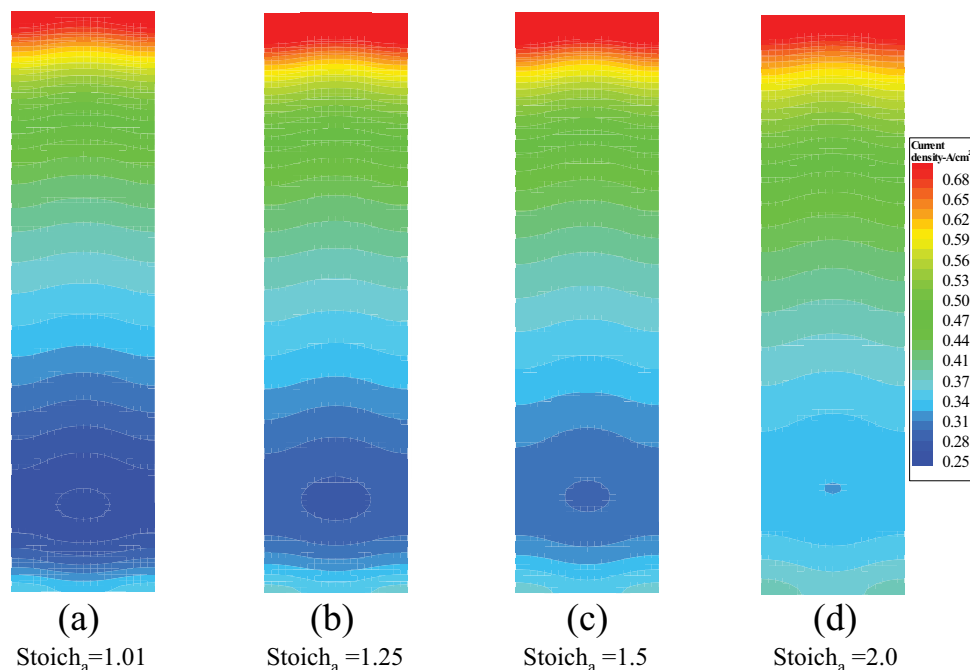


Figure 5. Current density distribution for $\text{stoich}_a = 1.01, 1.25, 1.5,$ and 2.0 at 0.7 V and $\text{RH}_{a/c} = 50\%/0\%$.

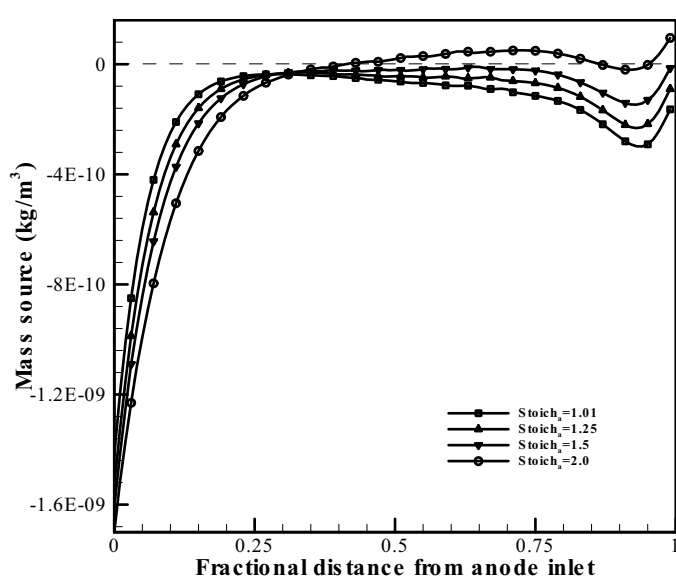


Figure 6. Mass sources in the anode catalyst layer for $\text{stoich}_a = 1.01, 1.25, 1.5,$ and 2.0 at 0.7 V and $\text{RH}_{a/c} = 50\%/0\%$.

Figure 6 presents the mass sources in the anode catalyst layer. The mass source is calculated by $S_m \times V$, where S_m and V are the source term in Eq. (1) and the local volume, respectively. The curve is primarily shaped by local water transport through the membrane (Wang and Wang 2005b). Note that the hydrogen electrochemical consumption usually contributes a small portion of this mass source. It can be seen that the anode loses a large amount of water to the cathode near the inlet for all the cases due to the dry cathode stream. In addition, the water loss under $\text{stoich}_a = 2.0$ is more than that under the ultrahigh fuel utilization due to more water contained in the anode inlet stream. Because fuel cell produces water, the anode gas flow channel will receive

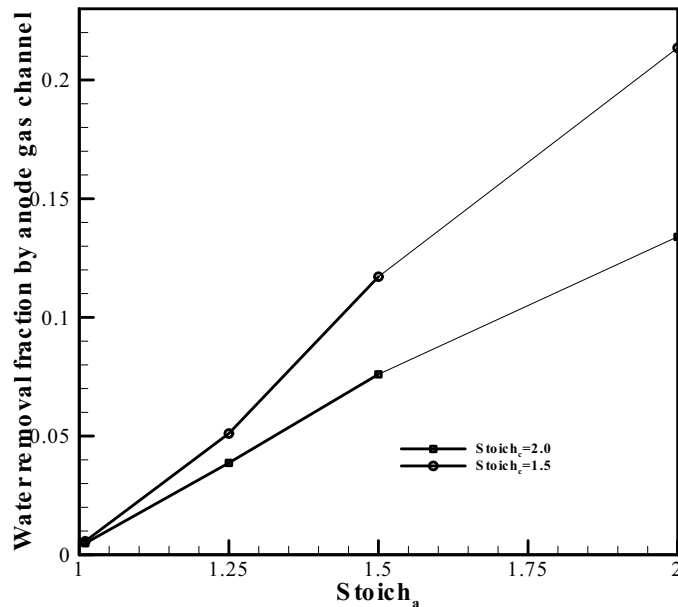


Figure 7. Water removal fraction by the anode gas channel for $\text{stoich}_c = 1.5$ and 2.0 , respectively, under 0.7 V and $\text{RH}_{a/c} = 50\%/0\%$.

water from water back-diffusion to compensate water loss due to the electroosmotic drag; thus, the anode mass loss decreases down the stream. For the case of $\text{stoich}_a = 2.0$, the mass source becomes positive as a result of the larger water back-diffusion rate which adds mass to the anode. For $\text{stoich}_a = 1.01$, nearly all the anode mass is lost to the cathode.

Since the anode stream decelerates to around zero under ultrahigh fuel utilization, water product removal will almost totally rely on the cathode stream. Figure 7 shows the water removal fraction by the anode stream. It can be seen that the anode stream removes about 13% of water for $\text{stoich}_a = 2.0$, while it has little contribution to water removal under the

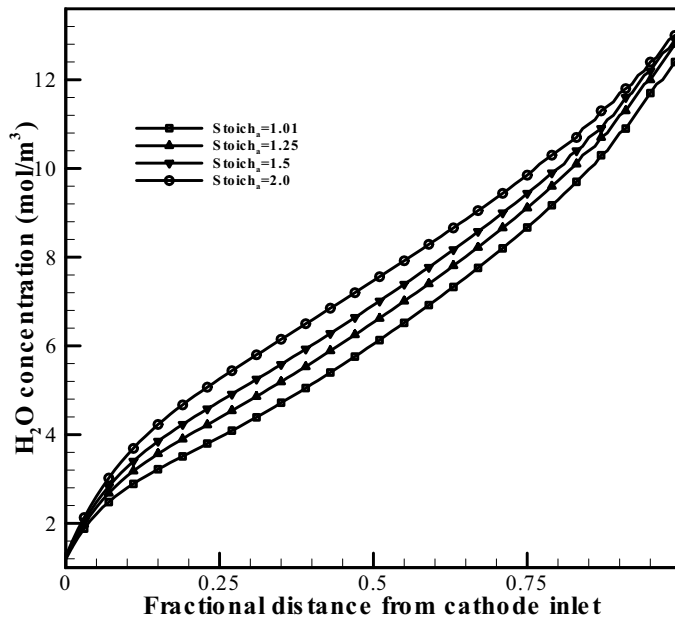


Figure 8. Average water concentration in the cathode channel under $\text{stoich}_c = 2.0$, 0.7 V and $\text{RH}_a/c = 50\%/0\%$.

Table 5. Simulation results at 0.7 V ($\text{RH}_a/c = 50\%/0\%$ and $\text{stoich}_c = 2.0$).

Stoich _a	Current density (A/cm ²)
2.0	0.44
1.5	0.43
1.25	0.42
1.01	0.40

ultrahigh fuel utilization. For the cathode stoichiometry ($\text{stoich}_c = 1.5$), the anode stream plays a more important role in water removal. For the ultrahigh fuel utilization strategy, a very small amount of water is removed by the anode flow, as expected, which may be a major reason for the enlarged instability regime as observed in the Part I experiment.

Figure 8 presents the average water vapor concentration in the cathode gas channel. It can be seen that the water concentration in the ultrahigh fuel utilization case is lower than the others, even though the water removal almost totally relies on the cathode flow. This is because that the anode inlet flow contains less amount of water for lower stoichiometry operation and a small portion of water is removed via the anode outlet. Figure 6 clearly indicates that much more water is lost to the cathode under $\text{stoich}_a = 2.0$ than the others. Under certain conditions, it is possible that the anode gas flow channel removes more water via its outlet than that it carries into the inlet. In such a case, the cathode water profiles may be different from those in Figure 8.

Figures 9 and 10 compare the polarization curves between the numerical prediction and experimental data. A good agreement is achieved and one can conclude that the ultrahigh fuel utilization has little effect on fuel cell performance in the stable operation regime. In addition, the Part I experiment observed an expanded unstable regime under the ultrahigh fuel utilization as shown in Figures 9 and 10. This can be explained by the fact that water removal will almost totally rely on the cathode channel flow, as shown in

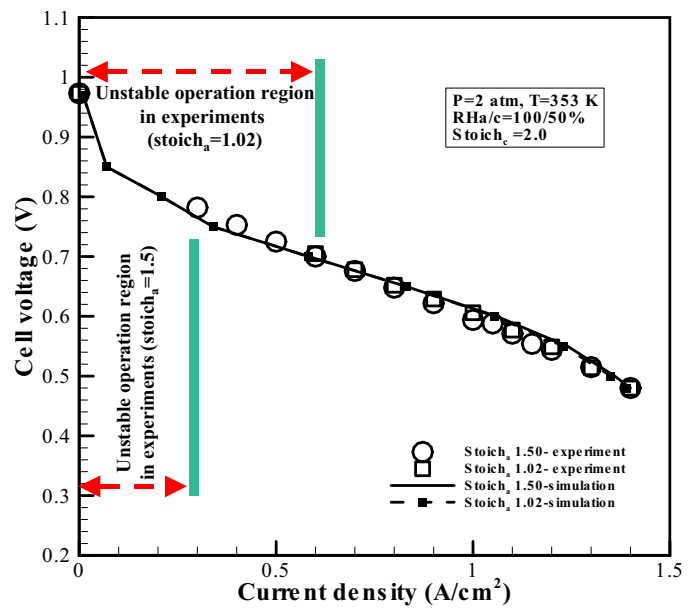


Figure 9. Comparison of the predicted polarization curve with experimental data for $\text{RH}_a/c = 100/50\%$.

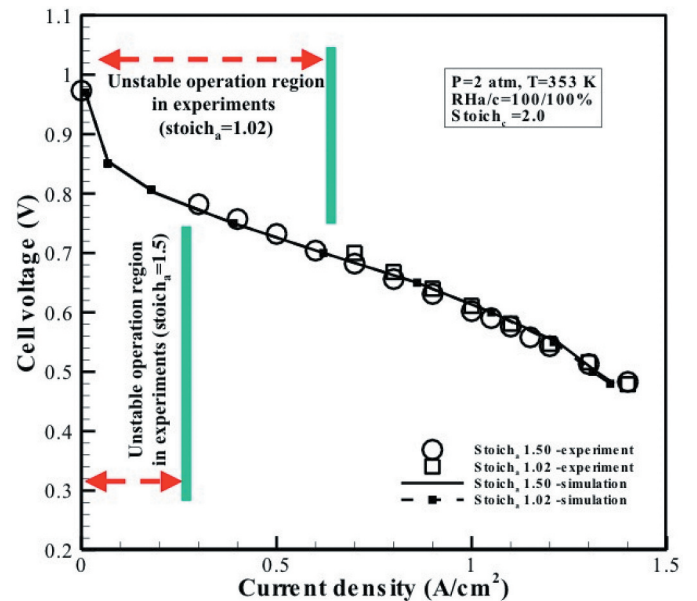


Figure 10. Comparison of the predicted polarization curve with experimental data for $\text{RH}_a/c = 100/100\%$.

Figure 7. Increasing the cathode stoichiometry or channel flow rate will mitigate the unstable operation, as pointed out by the Part I experiment. In addition, the anode flooding may be a reason as well. Figure 11 presents the water vapor profiles in the anode and cathode gas channels. It can be seen that the cathode curves are similar for $\text{stoich}_a = 1.02$ and 1.5. Near the anode outlet region, there is no remarkable difference in the water concentration; however, the values are above the saturate level for the two cases. Because the anode flow decelerates to around zero, the anode flooding becomes severe under $\text{stoich}_a = 1.02$. Note that the liquid droplets on the GDL surface are removed by the gas flow and the droplet detachment is positively correlated to the flow rate (Cho,

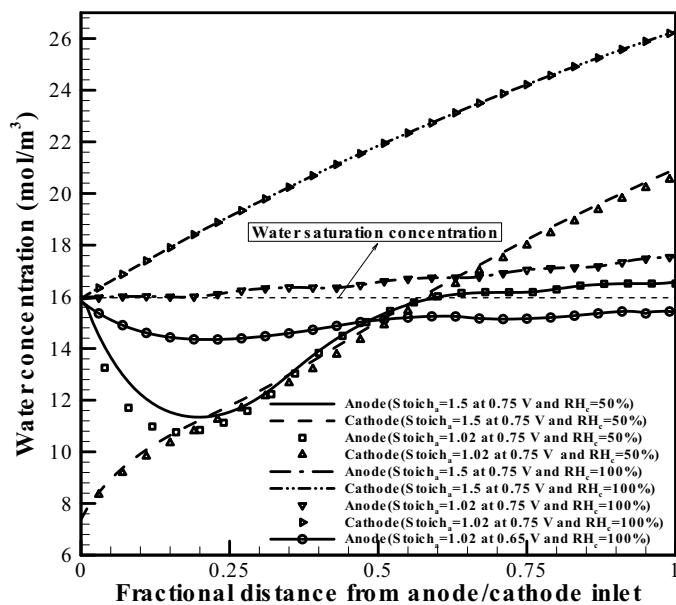


Figure 11. Water vapor concentration in the gas flow channels for $RH_{a/c} = 100/100\%$ and $100/50\%$, respectively.

Wang, and Chen 2012; Polverino, Esposito, and Pianese 2013). It may be difficult to evaluate the direct impact of anode flooding on fuel cell performance. However, the anode flooding will impact the cathode flooding through the water transport across the membrane. The latter will adversely affect the oxygen transport and oxygen reduction reaction (ORR) in the cathode. Again, by increasing the cathode gas flow rate or cathode stoichiometry, the cathode flooding can be mitigated. Figure 11 also presents the anode water profile under full humidity and a lower cell voltage (or a higher current density). In this case, the water vapor concentration remains lower than the saturation value due to the stronger water electro-osmotic drag. Even though the anode flow decelerates to around zero for the ultrahigh fuel utilization, its operation is stable under the low cell voltage or high current density due to depression of the anode flooding. In addition, under higher current density the cathode flow rate is larger, mitigating the flooding concerns.

4. Conclusions

3D numerical simulations of PEFCs were carried out to study ultrahigh fuel utilization ($>98\%$) using pure hydrogen fuel. As one of the first attempts to numerically investigate this strategy in detail, a dry operating condition was chosen under various anode stoichiometry including $stoich_a = 1.01$ (ultrahigh fuel utilization), 1.25, 1.5, and 2.0. The hydrogen concentration variation in the anode gas channel, water vapor concentration in the cathode gas channel, mass source in the anode catalyst layer, current density distribution, and water removal by the anode flow were presented and compared among these anode stoichiometries. Simulation results indicated that the anode gas flow under ultrahigh fuel utilization decelerated to around zero because almost all the hydrogen gas were consumed by the PEFC. The anode gas stream

remained high in the hydrogen concentration along the gas flow channel, eliminating any concerns of fuel starvation and increased anode overpotential. The simulation also confirmed the experimental observation that the ultrahigh fuel utilization has little effect on the fuel cell power output in the stable operation regime. Furthermore, it showed that the water removal in a fuel cell totally relied on the cathode gas flow under ultrahigh fuel utilization, which may be one major reason for the observed expanded range of instability operation. In addition, the anode flooding could be severe as the mass flow rate becomes low at the anode outlet due to the high fuel utilization and may contribute to the expanded unstable regime as observed in the Part I experiment.

Nomenclature

A	superficial electrode area, m^2
a	water activity; effective catalyst area per unit volume, m^2/m^3
C_k	molar concentration of species k, mol/m^3
D	mass diffusivity of species, m^2/s
EW	equivalent weight of dry membrane, kg/mol
F	Faraday's constant, $96,487 C/equivalent$
I	current density, A/cm^2
i_e	superficial current density, A/m^2
j	transfer current, A/cm^3
K	permeability, m^2
L	length, m
m	mass fraction
M	molecule weight, kg/mol
n	unit vector normal to a surface
n_d	electroosmosis coefficient, H_2O/H^+
P	pressure, Pa
Pe	Peclet number
R	universal gas constant, $8.134 J/mol K$
S	source term
s	stoichiometry coefficient in electrochemical reaction
t	time, s
T	temperature, K
U_o	equilibrium potential, V
\vec{u}	velocity vector, m/s
V_{cell}	cell potential, V
X	mole fraction
Greek	
α	transfer coefficient; net water flux per proton flux
ρ	density, kg/m^3
μ	viscosity, $kg/m s$
ϕ	phase potential, V
κ	ionic conductivity, S/m
ξ	stoichiometric flow ratio
λ	membrane water content
ϵ	porosity
η	surface overpotential, V
τ	shear stress, N/m^2
δ	thickness, m
Superscripts and Subscripts	
a	anode
c	cathode
CL	catalyst layer
e	electrolyte
eff	effective value
g	gas phase
GDL	gas diffusion layer
in	inlet
k	species
m	membrane phase
o	gas channel inlet value; reference value
ref	reference value
sat	saturate value
w	water

ORCID

Chao-Yang Wang  <http://orcid.org/0000-0003-0650-0025>

References

- Bergman, T. L., F. P. Incropera, D. P. DeWitt, and A. S. Lavine. 2011. *Fundamentals of heat and mass transfer*. John Wiley & Sons.
- Bird, R. B., W. E. Stewart, and E. N. Lightfoot. 2006. *Transport Phenomena*. John Wiley & Sons.
- Büchi, F., and G. G. Scherer. 2001. Investigation of the transversal water profile in nafion membranes in polymer electrolyte fuel cells. *Journal of the Electrochemical Society* 148:A183. doi:10.1149/1.1345868.
- Cho, S. C., Y. Wang, and K. S. Chen. 2012. Droplet dynamics in a polymer electrolyte fuel cell gas flow channel: Forces, Deformation and detachment. II: Comparisons of analytical solution with numerical and experimental results. *Journal of Power Sources* 210:191–97. doi:10.1016/j.jpowsour.2012.03.033.
- Demuren, A., and R. L. Edwards. 2020. Modeling Proton Exchange Membrane Fuel Cells—A Review. In *In 50 Years of CFD in Engineering Sciences*, 513–47. Singapore: Springer.
- Goshtasbi, A., B. L. Pence, and T. Ersal. 2016. Computationally efficient pseudo-2D non-isothermal modeling of polymer electrolyte membrane fuel cells with two-phase phenomena. *Journal of the Electrochemical Society* 163 (13):F1412–F1432. doi:10.1149/2.0871613jes.
- Jang, J. H., W. M. Yan, H. C. Chiu, and J. Y. Lui. 2015. Dynamic cell performance of kW-grade proton exchange membrane fuel cell stack with dead-ended anode. *Applied Energy* 142:108–14. doi:10.1016/j.apenergy.2014.12.073.
- Knight, S. D., K. D. Colbow, J. St-Pierre, and D. P. Wilkinson. 2004. Aging mechanisms and lifetime of PEFC and DMFC. *Journal of Power Source* 127:127. doi:10.1016/j.jpowsour.2003.09.033.
- Kone, J. P., X. Zhang, Y. Yan, G. Hu, and G. Ahmadi. 2017. Three-dimensional multiphase flow computational fluid dynamics models for proton exchange membrane fuel cell: A theoretical development. *The Journal of Computational Multiphase Flows* 9 (1):3–25. doi:10.1177/1757482X17692341.
- Kulikovsky, A. A. 2003. Quasi-3D Modeling of water transport in polymer electrolyte fuel cells. *J. Electrochem. Soc* 150:A1432. doi:10.1149/1.1611489.
- Kurnia, J. C., A. P. Sasmito, and T. Shamim. 2019. Advances in proton exchange membrane fuel cell with dead-end anode operation: A review. *Applied Energy* 252:113416. doi:10.1016/j.apenergy.2019.113416.
- Larminie, J., A. Dicks, and M. S. McDonald. 2003. *Fuel cell systems explained*, Vol. 2. Chichester, UK: J. Wiley.
- Matsuura, T., J. B. Siegel, J. Chen, and A. G. Stefanopoulou. Multiple degradation phenomena in polymer electrolyte fuel cell operation with dead-ended anode. In International Conference on Fuel Cell Science, Engineering and Technology (Vol. 54693, pp. 127–135) (2011, January).
- McKahn, D. A. 2015. Influence of gas channel depth in self-humidified miniature PEM fuel cells with dead-ended anode. *International Journal of Hydrogen Energy* 40 (22):7168–81. doi:10.1016/j.ijhydene.2015.02.132.
- Patankar, S. V. 1980. *Numerical Heat Transfer and Fluid Flow*. New York: Hemisphere Publishing Corp.
- Polverino, P., A. Esposito, and C. Pianese. 2013. Experimental validation of a lumped model of single droplet deformation, oscillation and detachment on the GDL surface of a PEM fuel cell. *International Journal of Hydrogen Energy* 38 (21):8934–53. doi:10.1016/j.ijhydene.2013.04.143.
- Song, G. H., and H. Meng. 2013. Numerical modeling and simulation of PEM fuel cells: Progress and perspective. *Acta Mechanica Sinica* 29 (3):318–34. doi:10.1007/s10409-013-0037-y.
- Springer, T. E., T. Rockward, T. A. Zawodinski, and S. Gottesfeld. 2001. Model for polymer electrolyte fuel cell operation on reformate feed: Effects of CO, H₂ dilution, and high fuel utilization. *Journal of the Electrochemical Society* 148 (1):A11. doi:10.1149/1.1344516.
- Sun, P., S. Zhou, Q. Hu, and G. Liang. 2012. Numerical study of a 3D two-phase PEM fuel cell model via a novel automated finite element/finite volume program generator. *Communications in Computational Physics* 11 (1):65–98. doi:10.4208/cicp.051010.180311a.
- Wang, C. Y. 2004. Fundamental models for fuel cell engineering. *Chemical Reviews* 104 (10):4727–66. doi:10.1021/cr020718s.
- Wang, Y., K. S. Chen, J. Mishler, S. C. Cho, and X. C. Adroher. 2011. A review of polymer electrolyte membrane fuel cells: Technology, applications, and needs on fundamental research. *Applied Energy* 88:981–1007.
- Wang, Y., and C. Y. Wang. 2005a. Simulations of flow and transport phenomena in a polymer electrolyte fuel cell under low-humidity operations. *Journal Power Source* 147:148–61. doi:10.1016/j.jpowsour.2005.01.047.
- Wang, Y., and C. Y. Wang. 2005b. Modeling polymer electrolyte fuel cells with large density and velocity changes. *Journal Electrochemical Society* 152:A445–A453. doi:10.1149/1.1851059.
- Wang, Y., and C. Y. Wang. 2006a. Ultra large-scale simulation of polymer electrolyte fuel cells. *Journal Power Source* 153 (1):130–35. doi:10.1016/j.jpowsour.2005.03.207.
- Wang, Y., and C. Y. Wang. 2006b. Dynamics of polymer electrolyte fuel cells undergoing load changes. *Electrochimica Acta* 51:3924–33. doi:10.1016/j.electacta.2005.11.005.
- Wilkinson, D. P., and J. St-Pierre. 2003. Durability. *Handbook of Fuel Cells: Fundamentals, Technology and Applications*, W. Vielstich, H. Gasteiger, and A. Lamm, ed., Vol. 3. 611. John Wiley & Sons, Ltd.
- Wu, H. W. 2016. A review of recent development: Transport and performance modeling of PEM fuel cells. *Applied Energy* 165:81–106. doi:10.1016/j.apenergy.2015.12.075.
- Yang, Y., X. Zhang, L. Guo, and H. Liu. 2017. Overall and local effects of operating conditions in PEM fuel cells with dead-ended anode. *International Journal of Hydrogen Energy* 42 (7):4690–98. doi:10.1016/j.ijhydene.2016.08.091.
- Zhou, J., D. Stanier, A. Putz, and M. Secanell. 2017. A mixed wettability pore size distribution based mathematical model for analyzing two-phase flow in porous electrodes II. Model validation and analysis of micro-structural parameters. *Journal of the Electrochemical Society* 164 (6):F540–F556. doi:10.1149/2.0391706jes.